Incremental Nonlinear Control for Aeroelastic Wing Load Alleviation and Flutter Suppression

Schildkamp, R.R.M.; Chang, J.; Sodja, J.; De Breuker, R.; Wang, Xuerui

INCREMENTAL NONLINEAR CONTROL FOR AEROELASTIC WING LOAD ALLEVIATION AND FLUTTER SUPPRESSION

Roderick Schildkamp[1]**, Jing Chang**[1]**, Jurij Sodja**[1]**, Roeland De Breuker**[1]**, Xuerui Wang**[1]

[1]Delft University of Technology
Kluyverweg 1, 2629 HS Delft
R.R.M.Schildkamp@tudelft.nl, J.Chang-2@tudelft.nl, J.Sodja@tudelft.nl
R.DeBreuker@tudelft.nl, X.Wang-6@tudelft.nl

Keywords: aeroservoelasticity, wind tunnel experiment, gust load alleviation, flutter suppression, nonlinear incremental control

Abstract: This paper proposes an incremental nonlinear control method for aeroelastic system gust load alleviation and active flutter suppression. These two control objectives can be achieved without modifying the control architecture or the control parameters. The proposed method has guaranteed stability in the Lyapunov sense and also has robustness against external disturbances and model mismatches. The effectiveness of this control method is validated by wind tunnel tests of an active aeroelastic parametric wing apparatus, which is a typical wing section containing heave, pitch, flap, and spoiler degrees of freedom. Wind tunnel experiment results show that the proposed nonlinear incremental control can reduce the maximum gust loads by up to 46.7% and the root mean square of gust loads by up to 72.9%, while expanding the flutter margin by up to 15.9%.

1 INTRODUCTION

Modern transport aircraft commonly feature high aspect ratio wings to increase aerodynamic efficiency. A disadvantage of increasing the wing aspect ratio is the increased susceptibility to gust and manoeuvre loads in addition to the onset of aeroelastic phenomena such as flutter and divergence. In the literature, there are typically two approaches to alleviate gust loads and suppress flutter: passive aeroelastic tailoring and active control [1]. The passive approach has a long history and is achieved by exploiting the anisotropic properties of composite material to steer dynamic and static aeroelastic behaviour. By contrast, the active approach designs feedforward and/or feedback controllers to actuate the leading-edge and/or trailing-edge control surfaces for load redistribution and closed-loop dynamic modification. This paper focuses on the active approach because typically, it has better adaptability to variations in flight and load conditions than its passive counterpart [1].

The majority of active gust load alleviation (GLA) and flutter suppression control algorithms are designed based on a reduced-order linear time-invariant state-space aero(servo)elastic model. These algorithms include the proportional–integral–derivative control [2], the pole placement [3], the linear quadratic regulator/Gaussian [4], eigensystem synthesis, μ analysis [5], linear robust control ($\mathcal{H}_2$ and $\mathcal{H}_\infty$ [6]). Although these linear control approaches have shown their effectiveness in practice, the resulting controllers only have guaranteed stability and performance around the linearization point, thus the additional and tedious gain-scheduling method [7] is required to expand these linear controllers to a wider flight envelope. Furthermore, it is challenging

for linear controllers to passively tolerate some specific nonlinearities (i.e., freeplay, backlash hysteresis [8], bifurcation [9]), sudden faults in actuators and/or sensors, and structure damage.

On the contrary, nonlinear control methods, especially those that have guaranteed stability in the Lyapunov sense, have shown great potential in solving nonlinear aeroservoelastic system control problems without requiring the gain scheduling technique. An immersion and invariance controller is proposed in [10] for nonlinear flutter suppression and free-play compensation. Platanitis et al. [11] uses the nonlinear dynamic inversion approach together with the model reference adaptive control technique for the limit cycle oscillation suppression of a typical aeroelastic wing section. Recurrent neural networks have been used for nonlinear model identification and active flutter suppression in [12]. However, these nonlinear control approaches have a relatively high model dependency, while offline and/or online model identification of a nonlinear aeroservoelastic system is a nontrivial task. When sudden faults occur during flight, the convergence rate of online model identification can be insufficient to guarantee stability.

Different from model-based nonlinear control methods in the literature, the incremental nonlinear dynamic inversion (INDI) control is a sensor-based approach [13]. It is derived from nonlinear dynamic inversion (NDI) or feedback linearization, which linearizes the input–output mapping of a nonlinear system via feedback, resulting in a chain of integrators that can be easily stabilized by a linear virtual control [13]. The INDI method inherits the merits of NDI. More importantly, it greatly reduces the model dependency of NDI via exploiting sensor measurement [13]. In conventional NDI, since a prefect model is never known and external disturbances always exist in reality, the ideal linearization never exists, leading to robustness issues. By contrast, INDI makes full use of sensing information and simultaneously reduces the model dependency and improves control robustness. In the literature, INDI has been applied to a free-flying flexible aircraft tracking problem [14] and a morphing wing gust load alleviation problem [15]. However, the effectiveness of INDI on flutter suppression, especially in a real-world environment remains to be proven.

In this paper, we propose to use the sensor-based incremental nonlinear dynamic inversion control to tackle the active gust load alleviation and flutter suppression problems of an aeroservoelastic system. The goal is to use one single controller to simultaneously achieve these two objectives without requiring gain adjustment, control architecture variations, or gain-scheduling. The reduced model-dependency of INDI also reduces its practical implementation effort. The performance, robustness, and implementation easiness of the proposed control method will be validated by wind tunnel experiments on our newly developed active aeroelastic parametric wing apparatus.

The rest of this paper is structured as follows. The main methods are detailed in Section 2. Section 3 explains the experimental setup. The results are presented and discussed Section 4, followed by the conclusion in Section 5. Finally, an outlook on future research is given in Section 6.

2 METHODS

2.1 Dynamic Model for a Typical Aeroelastic Wing Section

The equations of motion for a typical aeroelastic wing section can be written as

$$\begin{bmatrix} m & S & S_\beta \\ S & I_\theta & I_{\theta\beta} \\ S_\beta & I_{\theta\beta} & I_\beta \end{bmatrix} \begin{bmatrix} \ddot{h} \\ \ddot{\theta} \\ \ddot{\beta} \end{bmatrix} + \begin{bmatrix} K_h & 0 & 0 \\ 0 & K_\theta & 0 \\ 0 & 0 & K_\beta \end{bmatrix} \begin{bmatrix} h \\ \theta \\ \beta \end{bmatrix} = \begin{bmatrix} -L_h \\ M_\theta \\ M_\beta \end{bmatrix} \tag{1}$$

where h is the vertical displacement or plunge of the airfoil; θ is the pitch angle of the wing section; β is the deflection angle of the control surface; m is the mass per unit length of the wing section; S is the static mass moment of wing around the pitch axis; I_θ is its mass moment of inertial round the same axis. The static mass moment of the control surface around the hinge axis is denoted by S_β. I_β is the moment of inertia of the control surface around the hinge axis and $I_{\theta\beta}$ is the product of inertia. K_h, K_θ, K_β denote the extension spring of stiffness, the torsional spring of stiffness related to θ, and the torsional spring of stiffness related to β, respectively. L_h is the lift, M_θ is the pitching moment of wing section around the pitch axis, and M_β is the pitching moment of control surface around the hinge axis.

Considering unsteady aerodynamics, Theodorsen gives the complete expressions for the aerodynamic loads [16]. Using the exponential approximation of Wagner's function $\Phi(t) = 1 - \Psi_1 e^{-\epsilon_1 \frac{Ut}{b}} - \Psi_2 e^{-\epsilon_2 \frac{Ut}{b}}$ with $\Psi_1 = 0.165$, $\Psi_2 = 0.335$, $\epsilon_1 = 0.0455$ and $\epsilon_2 = 0.3$ [16], we obtain the complete equations of motion for a pitch-plunge airfoil with control surface as

$$(\boldsymbol{A} + \rho\boldsymbol{B})\ddot{\boldsymbol{y}} + (\boldsymbol{C} + \rho U\boldsymbol{D})\dot{\boldsymbol{y}} + (\boldsymbol{E} + \rho U^2\boldsymbol{F})\boldsymbol{y} + \rho U^3\boldsymbol{W}\boldsymbol{w} = \begin{bmatrix} -L_h & M_\theta & M_\beta \end{bmatrix}^\mathsf{T}_{\text{external}}$$
$$\dot{\boldsymbol{w}} = \boldsymbol{W}_1\boldsymbol{y} + U\boldsymbol{W}_2\boldsymbol{w} \tag{2}$$

where $\boldsymbol{y} = [h, \theta, \beta]^\mathsf{T}$ and $\boldsymbol{w} = [w_1, w_2, \ldots, w_6]^\mathsf{T}$ represents the aerodynamic lag states, ρ is the density of the flow, U is the speed of the flow. The external lift L_h and moments M_θ, M_β are induced by gust and control surface deflection.

The loads due to gust are represented as $[L_h^g, M_\theta^g, M_\beta^g]^\mathsf{T}$, in which the lift is purely circulatory event. The gust velocity u_g is implemented in circulatory lift calculations with Küssner function. The Küssner function is approximated with exponential form $\Psi(t) = 1 - \phi_1 e^{-\varepsilon_{k_1}\frac{Ut}{b}} - \phi_2 e^{-\varepsilon_{k_2}\frac{Ut}{b}}$ with $\phi_1 = 0.5$, $\phi_2 = 0.5$, $\varepsilon_{k_1} = 0.13$, $\varepsilon_{k_2} = 1$, where b is the half total chord of the airfoil and control surface. Define w_{g1} and w_{g2} as the aerodynamic lag states due to gust:

$$w_{g1} = \int_0^t e^{-\varepsilon_{k_1}(t-\tau)\frac{U}{b}} u_g(\tau)\mathrm{d}\tau, \quad w_{g2} = \int_0^t e^{-\varepsilon_{k_2}(t-\tau)\frac{U}{b}} u_g(\tau)\mathrm{d}\tau \tag{3}$$

After applying the Leibnitz integration rule and using the Küssner function, the complete expressions for the aerodynamic loads due to gust are defined as:

$$\dot{\boldsymbol{w}}_g = \begin{bmatrix} \dot{w}_{g1} \\ \dot{w}_{g2} \end{bmatrix} = \begin{bmatrix} -\frac{U\varepsilon_{k_1}}{b} & 0 \\ 0 & -\frac{U\varepsilon_{k_2}}{b} \end{bmatrix} \begin{bmatrix} w_{g1} \\ w_{g2} \end{bmatrix} + \begin{bmatrix} 1 \\ 1 \end{bmatrix} u_g \triangleq \boldsymbol{W}_{g1}u_g + U\boldsymbol{W}_{g2}\boldsymbol{w}_g$$

$$\boldsymbol{y}_g = \begin{bmatrix} -L_h^g \\ M_\theta^g \\ M_\beta^\theta \end{bmatrix} = 2\pi\rho U^2 \begin{bmatrix} -\phi_1\varepsilon_{k_1} & -\phi_2\varepsilon_{k_2} \\ -(a+0.5)b\phi_1\varepsilon_{k_1} & -(a+0.5)b\phi_2\varepsilon_{k_2} \\ \frac{bT_{12}}{2\pi}\phi_1\varepsilon_{k_1} & \frac{bT_{12}}{2\pi}\phi_2\varepsilon_{k_2} \end{bmatrix} \boldsymbol{w}_g \triangleq \boldsymbol{C}_g\boldsymbol{w}_g \tag{4}$$

where the parameter a and T_{12} are defined identical as in [16].

Assume that the inertial coupling force/moment for the control surface with regard to the rest of the wing section are negligible, then the independent servo actuator dynamics is governed by

$$\ddot{\beta} = -2\zeta_s\omega_s\dot{\beta} - \omega_s^2\beta + \omega_s^2\beta_c \tag{5}$$

where β_c is the control command for aileron, the coefficients ζ_s, ω_s are obtained using system identification of the servo .

3

Then, the dynamics for state $\bar{y} = [h, \theta]^T$ is governed by

$$(\bar{A} + \rho\bar{B})\ddot{\bar{y}} + (\bar{C} + \rho U\bar{D})\dot{\bar{y}} + (\bar{E} + \rho U^2\bar{F})\bar{y} + \rho U^3\bar{W}w = \begin{bmatrix} -L_h & M_\theta \end{bmatrix}^\mathsf{T}_{\text{external}}$$

$$\dot{w}_{1-4} = W_{1,1-4}\bar{y} + UW_{2,1-4}w_{1-4} \tag{6}$$

$$\dot{w}_{5-6} = W_{1,5-6}\beta + UW_{2,5-6}w_{5-6}$$

where $\bar{A}, \bar{B}, \bar{C}, \bar{D}, \bar{E}, \bar{F} \in \mathbb{R}^{2\times 2}$ and $\bar{W} \in \mathbb{R}^{2\times 6}$ are the corresponding matrices for h, θ fragmented from Eq. (2).

The resulting external force and moment due to the control surface deflection β are modeled as

$$\begin{bmatrix} L_h^\beta \\ M_\theta^\beta \end{bmatrix} = \begin{bmatrix} \rho U^2 F_{1,3} & \rho U D_{1,3} & \rho B_{1,3} \\ -\rho U^2 F_{2,3} & -\rho U D_{2,3} & -\rho B_{2,3} \end{bmatrix} \begin{bmatrix} \beta \\ \dot{\beta} \\ \ddot{\beta} \end{bmatrix} \tag{7}$$

where

$$F_{1,3} = 2bT_{10}\Phi(0) + \Xi b^2 T_{11}, \quad F_{2,3} = b^2(T_4 + T_{10}) - 2b^2(a + 0.5)T_{10}\Phi(0) - \Xi b^3(a + 0.5)T_{11}$$

$$D_{1,3} = -b^2 T_4 + \Phi(0)b^2 T_{11}, \quad D_{2,3} = b^3(T_1 - T_8 - (c_h - a)T_4 + 0.5T_{11}) - \Phi(0)b^3(a + 0.5)T_{11}$$

$$B_{1,3} = -b^3 T_1, \quad B_{2,3} = -b^4(T_7 + (c_h - a)T_1), \quad \Phi(0) = 1 - \psi_1 - \psi_2, \quad \Xi = \frac{\psi_1\epsilon_1}{b} + \frac{\psi_2\epsilon_2}{b}$$

and c_h, T_1 to T_{14} are defined identical as in [16].

With ignoring the inertia coupling between the aileron actuator and the rest of the wing section, and substituting Eq. (5) into Eq.(7), we have

$$\begin{bmatrix} -L_h^\beta \\ M_\theta^\beta \end{bmatrix} = \begin{bmatrix} -\rho U^2 F_{1,3} + \rho B_{1,3}\omega_s^2 & -\rho U D_{1,3} + 2\rho B_{1,3}\zeta_s\omega_s \\ -\rho U^2 F_{2,3} + \rho B_{2,3}\omega_s^2 & -\rho U D_{2,3} + 2\rho B_{2,3}\zeta_s\omega_s \end{bmatrix} \begin{bmatrix} \beta \\ \dot{\beta} \end{bmatrix} + \begin{bmatrix} -\rho B_{1,3}\omega_s^2 \\ -\rho B_{2,3}\omega_s^2 \end{bmatrix} \beta_c$$

$$\triangleq C_\beta \begin{bmatrix} \beta \\ \dot{\beta} \end{bmatrix} + D_\beta \beta_c \tag{8}$$

Now, choose state $x = [h, \theta, \dot{h}, \dot{\theta}, w^\mathsf{T}, \beta, \dot{\beta}, w_g^\mathsf{T}]^\mathsf{T}$, control output $y_c = h$, and control input $u = \beta_c$. The following control-oriented state-space model is obtained:

$$\dot{x}(t) = \mathcal{A}_c(t)x(t) + \mathcal{B}_c(t)u(t) + \mathcal{D}_c u_g(t) \tag{9}$$

where

$$\mathcal{A}_c = \begin{bmatrix} 0 & I_2 & 0 & 0 & 0 & 0 \\ -\bar{M}_{ae}^{-1}\bar{K}_{ae} & -\bar{M}_{ae}^{-1}\bar{C}_{ae} & -\bar{M}_{ae}^{-1}\rho U^3\bar{W}_{1-4} & -\bar{M}_{ae}^{-1}\rho U^3\bar{W}_{5-6} & \bar{M}_{ae}^{-1}C_\beta & \bar{M}_{ae}^{-1}\bar{C}_g \\ I_4 & 0 & UW_{2,1-4} & 0 & 0 & 0 \\ 0 & 0 & 0 & UW_{2,5-6} & I_2 & 0 \\ 0 & 0 & 0 & 0 & A_\beta & 0 \\ 0 & 0 & 0 & 0 & 0 & UW_{g2} \end{bmatrix}$$

$$\mathcal{B}_c = \begin{bmatrix} 0 & 0 & \bar{M}_{ae}^{-1}D_\beta & 0 & 0 & 0 & \omega_s^2 & 0 & 0 \end{bmatrix}^\mathsf{T}$$

$$\mathcal{D}_c = \begin{bmatrix} 0_{1\times 10} & 1 & 1 \end{bmatrix}^\mathsf{T} \tag{10}$$

with

$$\bar{M}_{ae} = \bar{A} + \rho\bar{B}, \quad \bar{K}_{ae} = \bar{E} + \rho U^2\bar{F}, \quad \bar{C}_{ae} = \bar{C} + \rho U\bar{D}$$

$$A_\beta = \begin{bmatrix} 0 & 1 \\ -\omega_s^2 & -2\zeta_s\omega_s \end{bmatrix}, \quad \bar{C}_g = 2\pi\rho U^2 \begin{bmatrix} -\phi_1\varepsilon_{k_1} & -\phi_2\varepsilon_{k_2} \\ -(a + 0.5)b\phi_1\varepsilon_{k_1} & -(a + 0.5)b\phi_2\varepsilon_{k_2} \end{bmatrix}$$

2.2 Incremental Nonlinear Dynamic Inversion

The Incremental Nonlinear Dynamic Inversion (INDI) method can control the following non-linear system:

$$\dot{\boldsymbol{x}} = \boldsymbol{f}(\boldsymbol{x}) + \boldsymbol{G}(\boldsymbol{x})\boldsymbol{u} + \boldsymbol{d}(t), \quad \boldsymbol{y} = \boldsymbol{h}(\boldsymbol{x}) \tag{11}$$

where $\boldsymbol{f} : \mathbb{R}^n \to \mathbb{R}^n$ and $\boldsymbol{h} : \mathbb{R}^n \to \mathbb{R}^p$ are smooth vector fields. $\boldsymbol{G}$ is a smooth function mapping $\mathbb{R}^n \to \mathbb{R}^{n \times m}$, whose columns are smooth vector fields. The external disturbance vector is $\boldsymbol{d}(t) \in \mathbb{R}^n$, which is assumed to satisfy $\|\boldsymbol{d}(t)\|_2 \le \bar{d}$. The external disturbances in the real-world can easily satisfy this boundedness assumption.

In Eq. (11), $\boldsymbol{y} \in \mathbb{R}^p$ denotes the controlled output vector. This paper considers the case where $p \le m$, which means the system is either full-actuated or over-actuated. The vector relative degree [17] of the system is defined as $\boldsymbol{\rho} = [\rho_1, \rho_2, ..., \rho_p]^\mathsf{T}$, which satisfies $\rho = \|\boldsymbol{\rho}\|_1 = \sum_{i=1}^p \rho_i \le n$. From Eq. (11), the input–output mapping of the nonlinear system is

$$\boldsymbol{y}^{(\boldsymbol{\rho})} = \boldsymbol{\alpha}(\boldsymbol{x}) + \boldsymbol{\mathcal{B}}(\boldsymbol{x})\boldsymbol{u} + \boldsymbol{d}_y \tag{12}$$

In Eq. (12), $\boldsymbol{\alpha}(\boldsymbol{x}) = [\mathcal{L}_f^{\rho_1} h_1, \mathcal{L}_f^{\rho_2} h_2, ..., \mathcal{L}_f^{\rho_p} h_p]^\mathsf{T}$, $\boldsymbol{\mathcal{B}}(\boldsymbol{x}) \in \mathbb{R}^{p \times m}$, $\mathcal{B}_{ij} = \mathcal{L}_{g_j} \mathcal{L}_f^{\rho_i - 1} h_i$, where $\mathcal{L}_f^{\rho_i} h_i$, $\mathcal{L}_{g_j} \mathcal{L}_f^{\rho_i - 1} h_i$ are the corresponding Lie derivatives [18]. When $\rho_i = 1$ for all $i = 1, ..., p$, $\boldsymbol{d}_y = [\mathcal{L}_d h_1, \mathcal{L}_d h_2, ..., \mathcal{L}_d h_p]^\mathsf{T}$. When $\rho = n$, then the system given by Eq. (11) is full-state feedback linearizable. Otherwise, $n - \rho$ internal dynamics exists.

INDI considers system variations in one sampling interval Δt. The incremental dynamic equation is derived by taking the first-order Taylor series expansion of Eq. (12) around the condition at $t - \Delta t$ (denoted by the subscript 0) as:

$$\boldsymbol{y}^{(\boldsymbol{\rho})} = \boldsymbol{y}_0^{(\boldsymbol{\rho})} + \left.\frac{\partial[\boldsymbol{\alpha}(\boldsymbol{x}) + \boldsymbol{\mathcal{B}}(\boldsymbol{x})\boldsymbol{u}]}{\partial \boldsymbol{x}}\right|_0 \Delta\boldsymbol{x} + \boldsymbol{\mathcal{B}}(\boldsymbol{x}_0)\Delta\boldsymbol{u} + \Delta\boldsymbol{d}_y + \boldsymbol{R}_1 \tag{13}$$

in which $\Delta\boldsymbol{x}$, $\Delta\boldsymbol{u}$, and $\Delta\boldsymbol{d}_y$ respectively represent the state, control, and disturbance increments in one sampling time step Δt. $\boldsymbol{R}_1$ is the expansion remainder. Define the internal state vector as $\boldsymbol{\eta} = \boldsymbol{\phi}(\boldsymbol{x})$ and the external state vector as $\boldsymbol{\xi} = [\boldsymbol{\xi}_1^\mathsf{T}, ..., \boldsymbol{\xi}_p^\mathsf{T}]^\mathsf{T}$, $\boldsymbol{\xi}_i = [h_i(\boldsymbol{x}), ..., \mathcal{L}_f^{\rho_i - 1} h_i(\boldsymbol{x})]^\mathsf{T}$, $i = 1, ..., p$. In a stabilization problem, the reference for the controlled output equals zero and the control increment is designed to satisfy

$$\bar{\boldsymbol{\mathcal{B}}}(\boldsymbol{x}_0)\Delta\boldsymbol{u}_{\text{indi}} = \boldsymbol{\nu}_c - \boldsymbol{y}_0^{(\boldsymbol{\rho})}, \quad \boldsymbol{\nu}_c = -\boldsymbol{K}\boldsymbol{\xi} \tag{14}$$

where $\bar{\boldsymbol{\mathcal{B}}}$ is an estimation of $\boldsymbol{\mathcal{B}}$. The gain matrix $\boldsymbol{K} = \text{diag}\{\boldsymbol{K}_i\}$, $i = 1, 2, ..., p$, and $\boldsymbol{K}_i = [K_{i,0}, ..., K_{i,\rho_i-1}]$. $\boldsymbol{y}_0^{(\boldsymbol{\rho})}$ can be directly measured or estimated. The total control command for actuator is $\boldsymbol{u}_{\text{indi}} = \boldsymbol{u}_{\text{indi},0} + \Delta\boldsymbol{u}_{\text{indi}}$, in which $\boldsymbol{u}_{\text{indi},0}$ can be measured or be estimated using an actuator model. Considering the internal dynamics, the resulting closed-loop dynamics are:

$$\begin{aligned} \dot{\boldsymbol{\eta}} &= \boldsymbol{f}_\eta(\boldsymbol{\eta}, \boldsymbol{\xi}, \boldsymbol{d}) = \left.\frac{\partial\boldsymbol{\phi}}{\partial\boldsymbol{x}}(\boldsymbol{f}(\boldsymbol{x}) + \boldsymbol{d}(t))\right|_{\boldsymbol{x}=\boldsymbol{T}^{-1}(\boldsymbol{z})} \\ \dot{\boldsymbol{\xi}} &= (\boldsymbol{A}_c - \boldsymbol{B}_c\boldsymbol{K})\boldsymbol{\xi} + \boldsymbol{B}_c[\boldsymbol{\delta}(\boldsymbol{x}, \Delta t) + (\boldsymbol{\mathcal{B}}(\boldsymbol{x}_0) - \bar{\boldsymbol{\mathcal{B}}}(\boldsymbol{x}_0))\Delta\boldsymbol{u}_{\text{indi}} + \Delta\boldsymbol{d}_y] \\ &\triangleq (\boldsymbol{A}_c - \boldsymbol{B}_c\boldsymbol{K})\boldsymbol{\xi} + \boldsymbol{B}_c\boldsymbol{\varepsilon}_{\text{indi}} \end{aligned} \tag{15}$$

where $\boldsymbol{z} = \boldsymbol{T}(\boldsymbol{x}) = [\boldsymbol{\eta}^\mathsf{T}, \boldsymbol{\xi}^\mathsf{T}]^\mathsf{T}$, is a diffeomorphism. The term $\boldsymbol{\delta}(\boldsymbol{x}, \Delta t)$ is the closed-loop value of the variations and expansion reminder:

$$\boldsymbol{\delta}(\boldsymbol{x}, \Delta t) = \left[\left.\frac{\partial[\boldsymbol{\alpha}(\boldsymbol{x}) + \boldsymbol{\mathcal{B}}(\boldsymbol{x})\boldsymbol{u}]}{\partial\boldsymbol{x}}\right|_0 \Delta\boldsymbol{x} + \boldsymbol{R}_1\right]\bigg|_{\boldsymbol{u}=\boldsymbol{u}_{\text{indi}}} \tag{16}$$

$\boldsymbol{A}_c = \text{diag}\{\boldsymbol{A}_0^i\}$, $\boldsymbol{B}_c = \text{diag}\{\boldsymbol{B}_0^i\}$, $\boldsymbol{C}_c = \text{diag}\{\boldsymbol{C}_0^i\}$, $i = 1, 2, ..., p$, and $(\boldsymbol{A}_0^i, \boldsymbol{B}_0^i, \boldsymbol{C}_0^i)$ is the canonical form representation of a chain of ρ_i integrators. The gain matrix $\boldsymbol{K}$ is designed to guarantee that $\boldsymbol{A}_c - \boldsymbol{B}_c \boldsymbol{K}$ is Hurwitz [13].

Theorem 1 *If $\|\boldsymbol{\varepsilon}_{indi}\|_2 \leq \bar{\varepsilon}$ is satisfied for all $\boldsymbol{\xi} \in \mathbb{R}^\rho$, $\boldsymbol{f}_\eta(\boldsymbol{\eta}, \boldsymbol{\xi}, \boldsymbol{d})$ is continuously differentiable and globally Lipschitz in $(\boldsymbol{\eta}, \boldsymbol{\xi}, \boldsymbol{d})$, and the origin of $\dot{\boldsymbol{\eta}} = \boldsymbol{f}_\eta(\boldsymbol{\eta}, \boldsymbol{0}, \boldsymbol{0})$ is globally exponentially stable, then the external state $\boldsymbol{\xi}$ in Eq. (15) is globally ultimately bounded by a class $\mathcal{K}$ function of $\bar{\varepsilon}$, while the internal state $\boldsymbol{\eta}$ in Eq. (15) is globally ultimately bounded by a class $\mathcal{K}$ function of $\bar{\varepsilon}$ and $\bar{d}$.*

Proof: This can be proved by applying the Theorem 1 in Ref. [15] and setting the reference vector to zero.

Theorem 2 *If $\|\boldsymbol{\varepsilon}_{indi}\|_2 \leq \bar{\varepsilon}$ is satisfied for all $\boldsymbol{\xi} \in \mathbb{R}^\rho$, $\boldsymbol{f}_\eta(\boldsymbol{\eta}, \boldsymbol{\xi}, \boldsymbol{d})$ is continuously differentiable, and the origin of $\dot{\boldsymbol{\eta}} = \boldsymbol{f}_\eta(\boldsymbol{\eta}, \boldsymbol{0}, \boldsymbol{0})$ is exponentially stable, then there exists a neighborhood D_z of $\boldsymbol{z} = \boldsymbol{0}^\mathsf{T}$ and $\varepsilon^* > 0$, such that for every initial state $\boldsymbol{z}(0) \in D_z$ and $\bar{\varepsilon} < \varepsilon^*$, the external state $\boldsymbol{\xi}$ in Eq. (15) is ultimately bounded by a class $\mathcal{K}$ function of $\bar{\varepsilon}$, while the internal state $\boldsymbol{\eta}$ in Eq. (15) is ultimately bounded by a class $\mathcal{K}$ function of $\bar{\varepsilon}$ and $\bar{d}$.*

Proof: This can be proved by applying the Theorem 2 in Ref. [15] and setting the reference vector to zero.

Theorems 1 and 2 prove that under the perturbation of bounded uncertainties and disturbances and with stable internal dynamics, the closed-loop system under INDI control is stable in the Lyapunov sense.

2.3 INDI Design for an Aeroelastic Wing

In this research, we focus on stabilizing the heave degree of freedom of the aeroelastic wing using the trailing-edge flap. Consequently, in Eq. (9), the controlled output is h, while the input $u = \beta_c$. This leads to an input–output mapping with relative degree equals two. Applying Eq. (14), the aileron input for stabilization is designed as:

$$\Delta u_{\text{indi}} = (\nu_c - \ddot{h}_0)/\bar{\mathcal{B}}(\boldsymbol{x}_0), \quad \nu_c = -K_d \dot{h} - K_p h \tag{17}$$

where $K_d > 0$ and $K_p > 0$ are differential and proportional gains. The aileron control input command equals $\beta_c = u_{\text{indi}} = u_{\text{indi},0} + \Delta u_{\text{indi}}$, in which $u_{\text{indi},0}$ is the control input at the previous time point.

In Sec. 3, we will validate the performance of the INDI method for gust load alleviation and active flutter suppression challenges. It is noteworthy that this one single controller can solve both issues without changing the control architecture or the control gains.

3 EXPERIMENT SETUP

The proposed controller for active gust load alleviation and flutter suppression was validated using an aeroelastic wing apparatus by wind-tunnel testing. The self-designed active wing section [19] itself is mounted in an aeroelastic apparatus (AA) developed by Gjerek et al. [20].

The AA consists of a rectangular, acrylic section that is mounted to the gust generator and provides heave and pitch degrees of freedom, with adjustable stiffness. In addition to the adjustable stiffness, weights can be added forward or rearwards of the pitch axis, allowing both the mass distribution of the wing to be easily changed. The wing section is equipped with a movable full-span trailing-edge control surface (aileron) and a spoiler, which are actuated by high-bandwidth, electric servo actuators. The main focus of this experiment is to use the aileron for controlling the heave degree of freedom. The wing is also equipped with an MPU-9250 inertial measurement unit (IMU), as well as linear and rotation variable differential transformers (LVDT - Sentech 75DC-500/RVDT - Midori QP-2HC) for the measurements of acceleration, angular rates, heave, and pitch. All combined, this AA provides a setup that closely resembles the typical section, a two-dimensional wing section with an aileron and heave and pitch degrees of freedom (DOFs), in combination with the aerodynamic model developed by Theodorsen [21], which has been presented in Section 2.1.

Wind tunnel testing was performed at the low-speed W-tunnel at Delft University of Technology, which is an open-circuit blow-down tunnel with a $0.4 \, \text{m} \times 0.4 \, \text{m}$ test section, with low turbulence levels and a maximum attainable speed of $35 \, \text{m/s}$[a]. Attached to the wind tunnel is a gust generator capable of generating sinusoidal and 1-cosine gust excitations with gust frequencies ranging from $0.5 \, \text{Hz}$ to $12 \, \text{Hz}$ in $0.5 \, \text{Hz}$ increments [22].
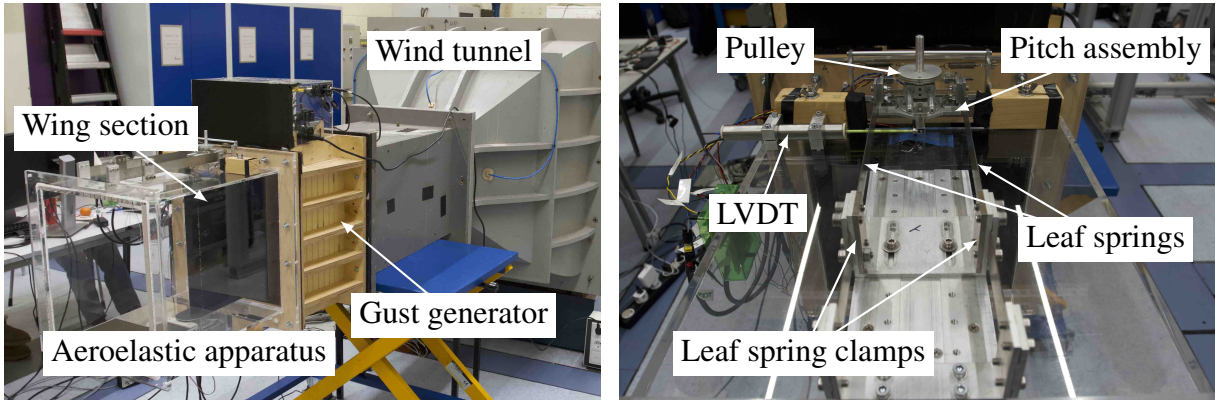
(a) Wind tunnel with the gust generator and aeroelastic apparatus.

(b) Top view of the aeroelastic apparatus. Note, the RVDT is placed on the bottom side.

Figure 1: Overview of the test setup.

The heave DOF is provided by two pairs of cantilever leaf springs, with one end of the springs clamped to the AA and the other end connected to a pitch assembly. The axles protruding from both sides of the wing are connected to bearings in the pitch assembly. The length of the leaf springs can be changed, providing a variable spring stiffness in the heave. Torsional stiffness is provided by a pair of axial springs connected to one of the axles by a pulley. The torsional stiffness can be varied by changing the diameter of the pulley or exchanging the axial springs. A top view of the AA is seen in Figure 1b, showing the top half of the heave and pitch mechanism.

The specifications of the aeroelastic wing apparatus for GLA and flutter suppression are shown in Table 1. When the blades of gust generator deflect at a certain frequency, gusts are generated in the wing section test field with gust induced angle of attack $\alpha_g = \frac{1}{2} A_{g0} a_m (1 - \cos(2\pi f_g (t - t_0)))$, where t_0 is the initial time, a_m is the amplitude of the blades deflection angle, A_{g0} is the

---

[a]https://www.tudelft.nl/lr/organisatie/afdelingen/aerodynamics-wind-energy-flight-performance-and-propulsion/facilities, accessed on April 27, 2022

gust coefficient relevant to the velocity U and the gust generator frequency f_g. A second-order model for the aileron actuation mechanism is given by $G_{\text{act}}(s) = \frac{2.6s+347.8}{s^2+34.7s+358.3}$. The minimal and maximal deflections are limited to $-20°$ and $20°$, and the maximum deflection rate is estimated to be $750°/s$. The IMU used on the apparatus has a bandwidth of $200\,\text{Hz}$. The LVDT has a cutoff frequency of $200\,\text{Hz}$ and is read by a 12-bit analog-to-digital converter, resulting in a resolution of approximately $6 \times 10^{-3}\,\text{mm}$. The sampling interval is set as $0.002\,\text{s}$ for capturing the high-frequency aeroelastic modes. The measured outputs used by the controller are heave acceleration $\ddot{h}$ from IMU, heave displacement h from LVDT, and control surface deflection β_0.

Table 1: Configuration parameters of the aeroelastic apparatus.

Parameter		Value	Unit
Heave stiffness	K_h	710	N/m
Pitch stiffness	K_θ	3.14	Nm/rad
Elastic Axis	EA	$0.4c$	–

4 RESULTS AND DISCUSSION

In this section, the experimental results will be discussed. First, the GLA results are presented in Section 4.1. Then this is followed by the flutter suppression results in Section 4.2.

4.1 Gust load alleviation results

The GLA results are presented in this subsection. In the wind tunnel test, $K_p = 0.12$, $K_d = 0.009$ are chosen for the controller gains based on the desired eigenvalues of the closed-loop system. The nominal control effectiveness for $12\,\text{m/s}$ is identified from a wind tunnel test as $\hat{\mathcal{B}} = 4.0$. The open- and closed-loop experiments were performed for gust frequencies f_g of $3\,\text{Hz}$, $3.5\,\text{Hz}$, $4\,\text{Hz}$, $4.5\,\text{Hz}$ and $5\,\text{Hz}$, and gust amplitude of $a_m = 15\,\text{deg}$. In addition to the directly measured outputs $\ddot{h}$ and h from the IMU and LVDT, a Luenberger observer with eigenvalues $[-150, -30]$ is applied to provide an estimation of $\dot{\hat{h}}$ by using the measurements of heave displacement and acceleration. $\dot{\hat{h}}$ is needed for the implementation of control law as shown in Eq. (17). An overview of the measured and estimated signals is shown in Figure 2.
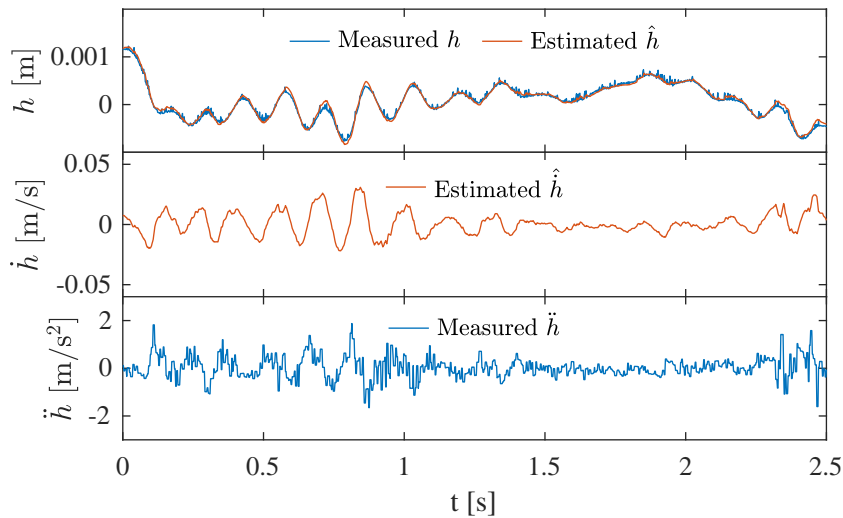

Figure 2: Overview of the measured and estimated signals.

For the GLA experiments, the wing was subjected to a series of 1-cosine gusts. First, the open-loop gust response was determined, after which the experiment was repeated with the controller

enabled. Figure 3 shows the recorded GLA data for gust frequencies of $3\,\mathrm{Hz}$, $4\,\mathrm{Hz}$ and $5\,\mathrm{Hz}$. The results show significant improvements in reducing the amplitude of h. The top plot of each sub-figures shows the theoretical gust input in terms gust-induced angle of attack α_g. At each frequency, the experiments were repeated four times for evaluating the coherence of the results.
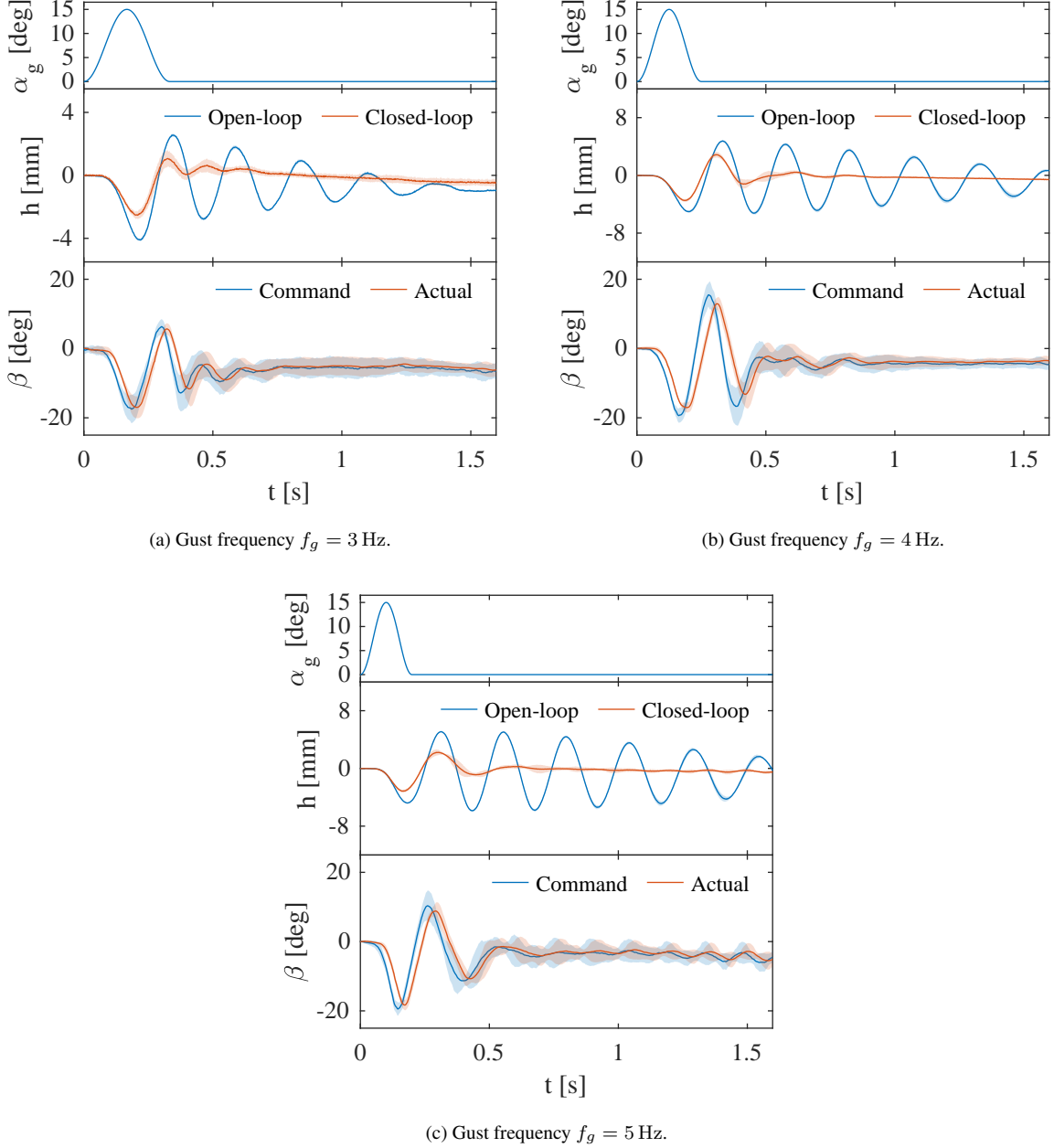

(a) Gust frequency $f_g = 3\,\mathrm{Hz}$.

(b) Gust frequency $f_g = 4\,\mathrm{Hz}$.

(c) Gust frequency $f_g = 5\,\mathrm{Hz}$.

Figure 3: Overview of the mean GLA results for different gust frequencies, flow velocity $U = 13.5\,\mathrm{m/s}$.

The middle subplots show comparisons of the mean values of the open-loop (in dashed) and closed-loop responses (in solid). Also included in each one of the middle subplots is the standard deviation of the heave response as a shaded region, which nearly coincides with the mean data, proving the coherence and repeatability of the experimental results. The transient open-loop heave response in the middle plots can be subdivided into two parts. During the first half period of the oscillation, the response is dominated by the gust input. For the remainder of the transient response, the wing oscillates with a frequency of approximately $4\,\mathrm{Hz}$, close to the frequency of the first heave mode of the wing section. Where the open-loop results are highly

underdamped, the closed-loop responses are mostly damped out after one full period.

The commanded and actual aileron deflections are detailed in the bottom subplots Figure 3. It can be observed that the aileron is settled on a steady-state deflection after the convergence of heave response. Results from Schildkamp et al. [19] show the magnitude and phase responses of the servo actuator degrades for frequencies higher than 2 Hz. Since the servo actuator is now connected to the aileron, adding inertia and friction to the system, the frequency response is expected to be worse than what was presented in [19]. The commanded aileron deflection has a frequency similar to that of the heave response, explaining the differences in magnitude and phase between the commanded and actual aileron deflection. The larger variability seen in both aileron deflection signals are attributed to noise in the signals driving the controller.

A summary of GLA results in terms of the reduction of absolute peak value and RMS heave values for all previously mentioned gust frequencies is shown in Table 2, where the absolute peak heave value relates to the peak load endured by the wing, and the RMS value gives a measure of the vibrational loads the wing endures, relating to the fatigue life of a structure. The mean, minimum, and maximum reduction rates for both the absolute peak and RMS values are given. Overall, the proposed INDI control method, without adjusting control gains, provides attenuation higher than 27% for vibration amplitude due to gust disturbance, and attenuation of higher than 44% for the RMS(h). The greatest reduction in absolute peak and RMS mean values are achieved for a gust frequency of 5 Hz, respectively 71.4% and 44.2%. Previous results show the overall lowest damping coefficient for the open-loop gust response at 5 Hz, giving the highest RMS value. The controller quickly damps out the gust-induced oscillations, leading to the second-lowest closed-loop RMS value, hence the greatest reduction in RMS. Similarly, this is also the case for the absolute peak value, with the highest open-loop peak value and the second lowest peak value.

Table 2: GLA controller reduction rate of the heave displacement h.

f_g [Hz]	Reduction rate of $\max(|h|)$ [%]			Reduction rate of RMS(h) [%]		
	mean	min	max	mean	min	max
3	38.3	33.8	44.6	51.1	46.0	54.5
3.5	29.3	27.0	30.8	58.7	58.7	59.7
4	32.4	31.5	34.4	63.5	61.2	64.1
4.5	33.2	29.8	35.8	61.7	44.0	67.4
5	44.2	40.6	46.7	71.4	63.0	72.9

In addition to the open- and closed-loop heave responses plotted in the time domain, Figure 4 shows the power spectral density (PSD) of these heave responses in the frequency domain for gust frequencies of 3 Hz, 4 Hz and 5 Hz. Also indicated in this figure are the (1) first heave mode, (2) first pitch mode, and (3) first rocking mode at 3.55 Hz, 6.39 Hz and 11.10 Hz respectively, as identified using a ground vibration test (GVT) described in [19]. The open-loop results in two distinct peaks, around 4 Hz and 12 Hz, at frequencies slightly higher than first heave and rocking modes. Changes to the hardware and wiring of the wing section were made after the GVT, likely affecting the identified frequencies. This will be verified during a future GVT.

Three observations can be made from the closed-loop PSDs. First, as expected, the energy near the heave and rocking modes is reduced as the heave motion is primarily influenced by the use of the controller. Secondly, an increase in energy can be seen near the first pitch mode. This result

is also expected, as the implemented controller does not directly damp out the pitch mode and it is well-known that if a trailing-edge control device is used for GLA, then the root bending moment is alleviated with an expense of the amplification in the root torsional moment [23]. Furthermore, deflecting the aileron not only induces a heave motion, but also a pitching motion around the elastic axis. Finally, no differences can be observed for frequencies greater than $15\,\mathrm{Hz}$ owing to the finite actuator bandwidth.
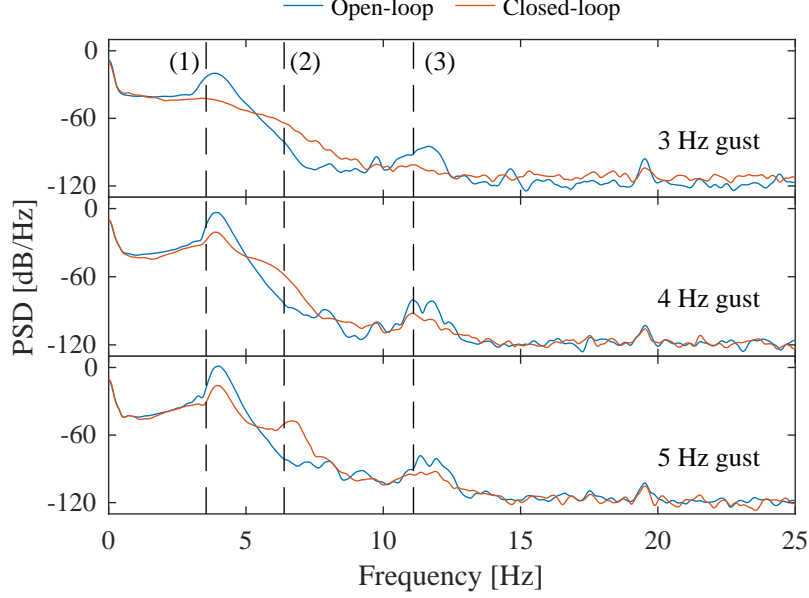

Figure 4: Heave PSD comparison for gust frequencies of $3\,\mathrm{Hz}$, $4\,\mathrm{Hz}$ and $5\,\mathrm{Hz}$.

4.2 Flutter suppression results

In this subsection, we evaluate the flutter suppression ability of the INDI controller designed in Eq. (17). Both the control architecture and control gains (K_p, K_d) were kept the same as in the GLA experiment. It is noteworthy that the control effectiveness $\bar{\mathcal{B}}(\boldsymbol{x}_0)$ is a function of dynamic pressure. Therefore, it is scaled by U^2 during the experiment. The static flow velocity U is known and is converted from the tunnel RPM value. The open-loop flutter speed was determined to be $U_f = 14.5\,\mathrm{m/s}$ using the parametric flutter margin method [19]. Moreover, the control reversal speed was also determined for this configuration as $U_R = 14.4\,\mathrm{m/s}$, which is slightly below the flutter speed.

To test the performance of the controller for flutter suppression, the flow velocity is gradually increased in steps past the flutter speed up to a velocity of $18.5\,\mathrm{m/s}$. At each velocity step, the wing section is excited from its equilibrium position to trigger flutter. For consistent excitations of the wing section, it is subjected to a pre-defined 1-cosine gust. First, open-loop flutter is recorded. To prevent any damage to the wing section or test setup, the wing section is manually stopped and returned to its equilibrium position after flutter occurs. The manual stopping of the wing is visible in the plotted gust responses by clipping and sharp peaks in the heave responses seen in Figures 5c and 5d. After recording the open-loop flutter, the controller is activated and the wing section is excited again to record the closed-loop flutter response.

Figure 5 shows a comparison of the open- and closed-loop heave response and the commanded and actual aileron deflection for the closed-loop response for increasing flow velocities past the open-loop flutter velocity. All open-loop responses to the excitation start with a $5\,\mathrm{mm}$ amplitude

11

(a) Flow velocity $U = 13.1 \, \mathrm{m/s}$.

(b) Flow velocity $U = 14.6 \, \mathrm{m/s}$.

(c) Flow velocity $U = 15.4 \, \mathrm{m/s}$.

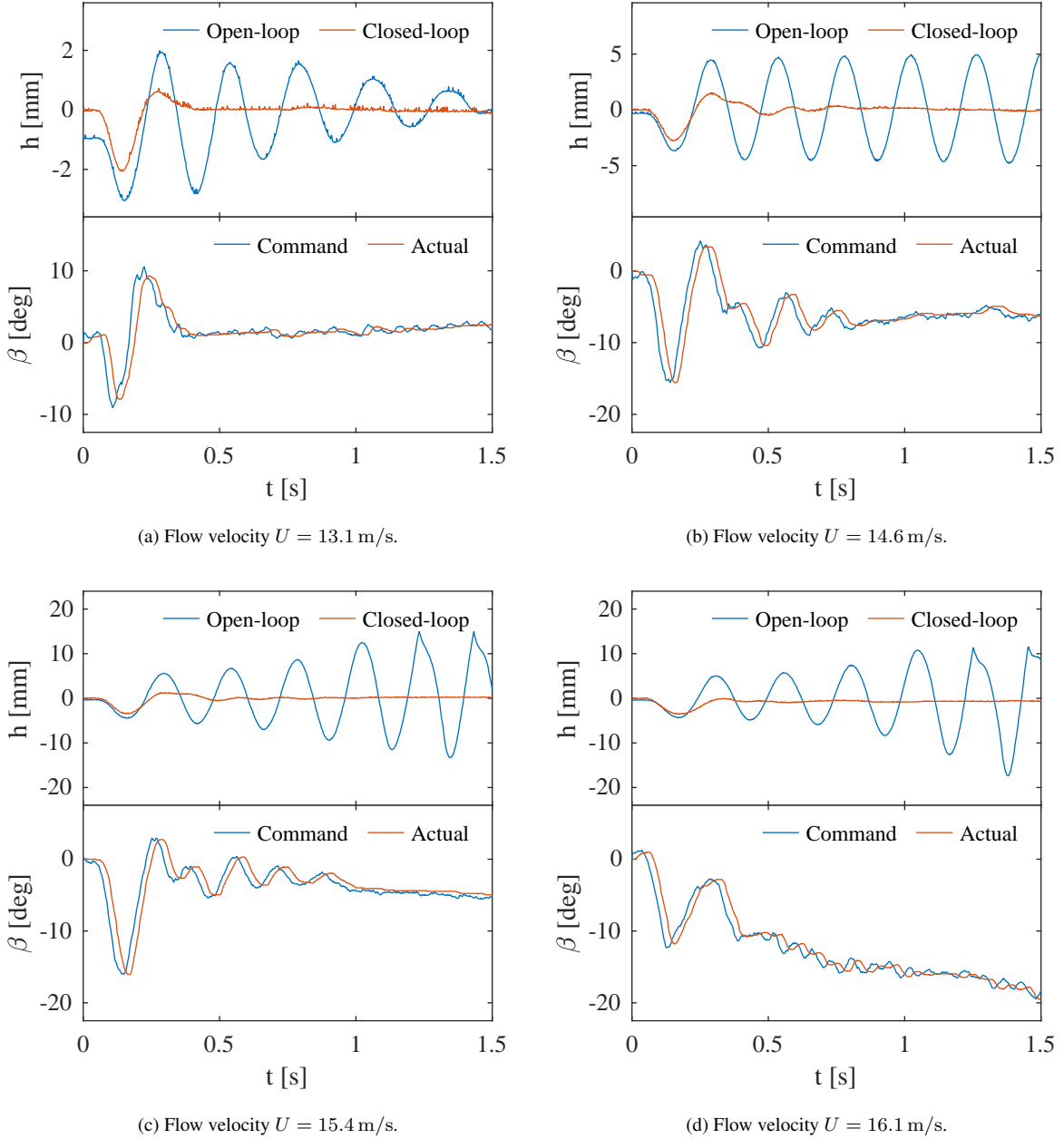(d) Flow velocity $U = 16.1 \, \mathrm{m/s}$.

Figure 5: Comparisons of the open- and closed-loop heave responses and commanded and actual aileron deflections.

and expectedly oscillate with a frequency around $4 \, \mathrm{Hz}$, again close to the first heave mode. Figures 5c and 5d show a clear diverging open-loop response. The closed-loop responses show the reduction of the heave response to the initial excitation compared to the open-loop response, after which the disturbance is damped out within approximately one period.

Similar to the GLA results, the actual aileron deflection shows a slight lag in time of $0.02 \, \mathrm{s}$. For the higher velocities, Figures 5c and 5d, a non-zero aileron deflection can be observed after the initial disturbance has been damped out. Since the test conditions are beyond the control reversal speed, the heave response however remains constant, indicating that the controller has found a new equilibrium position where the increment in lift due to the aileron deflection is offset by the decrement in lift due to the change in pitch of the wing section.

Overall, the flutter suppression tests have shown the implemented INDI controller is able to increase the closed-loop flutter speed to $16.8 \, \text{m/s}$, an increase of $15.9\,\%$.

5 CONCLUSION

In this paper, we designed a single nonlinear controller for the gust load alleviation and active flutter suppression problems of a typical wing section. The effectiveness of the proposed incremental nonlinear dynamic inversion (INDI) controller has been validated by wind tunnel tests.

The GLA performance of the INDI controller was tested by subjecting the wing section to gust frequencies of $3 \, \text{Hz}$, $3.5 \, \text{Hz}$, $4 \, \text{Hz}$, $4.5 \, \text{Hz}$ and $5 \, \text{Hz}$. Time domain analyses of the results show a reduction in peak heave displacement of up to 46.7% and a reduction in heave RMS of up to 72.9%. Frequency domain results show a decrease in energy near the first heave and rocking modes compared to the open-loop, while an increase in energy is observed near the first pitch mode. This is expected as the controller focuses on damping out the heave motion and it is well-known that the use of a trailing-edge control device typically amplifies pitch motions.

The effectiveness of the proposed INDI controller on flutter suppression is also validated by wind tunnel experiments. Neither the control architecture nor the control parameters need to be changed. The open-loop flutter speed was found at $U_f = 13.5 \, \text{m/s}$. Using the INDI controller, the flutter speed was increased to $16.8 \, \text{m/s}$, achieving an increase of 15.9%.

6 OUTLOOK

In this research, we focus on alleviating gust responses and suppressing flutter in the heave degrees of freedom. We have planned future wind tunnel tests for including pitch degree of freedom in the feedback signal and will explore the harmonious usage of both aileron and spoiler. Furthermore, we plan to include automatic adaptation to the INDI controller, which enables it to self-adapt to variations in free streaming velocities.

7 REFERENCES

[1] Binder, S., Wildschek, A., and De Breuker, R. (2021). The interaction between active aeroelastic control and structural tailoring in aeroservoelastic wing design. *Aerospace Science and Technology*, 110, 106516. ISSN 12709638. doi:10.1016/j.ast.2021.106516.

[2] Ricci, S., Scotti, A., Cecrdle, J., et al. (2008). Active control of three-surface aeroelastic model. *Journal of Aircraft*, 45(3), 1002–1013. ISSN 15333868. doi:10.2514/1.33303.

[3] Karpel, M. (1982). Design for Active Flutter Suppression and and Gust Alleviation Using State-Space Aeroelastic Modeling. *Journal of Aircraft*, 19(March), 221–227.

[4] Nguyen, N. T., Swei, S., and Ting, E. (2015). Adaptive Linear Quadratic Gaussian Optimal Control Modification for Flutter Suppression of Adaptive Wing. In *AIAA Infotech @ Aerospace*. Kissimmee, Florida: American Institute of Aeronautics and Astronautics. ISBN 978-1-62410-338-4, pp. 1–23. doi:10.2514/6.2015-0118.

[5] Fournier, H., Massioni, P., Tu Pham, M., et al. (2022). Robust Gust Load Alleviation of Flexible Aircraft Equipped with Lidar. *Journal of Guidance, Control, and Dynamics*, 45(1), 58–72. ISSN 1533-3884. doi:10.2514/1.G006084.

[6] Poussot-Vassal, C., Demourant, F., Lepage, A., et al. (2017). Gust Load Alleviation: Identification, Control, and Wind Tunnel Testing of a 2-D Aeroelastic Airfoil. *IEEE Transactions on Control Systems Technology*, 25(5), 1736–1749. ISSN 10636536. doi: 10.1109/TCST.2016.2630505.

[7] Lhachemi, H., Chu, Y., Saussié, D., et al. (2017). Flutter Suppression for Underactuated Aeroelastic Wing Section: Nonlinear Gain-Scheduling Approach. *Journal of Guidance, Control, and Dynamics*, 40(8), 2102–2109. ISSN 0731-5090. doi:10.2514/1.G002497.

[8] Sun, B., Mkhoyan, T., Van Kampen, E.-J., et al. (2022). Vision-based nonlinear incremental control for a morphing wing with mechanical imperfections. *IEEE Transactions on Aerospace and Electronic Systems*.

[9] Livne, E. (2018). Aircraft active flutter suppression: State of the art and technology maturation needs. *Journal of Aircraft*, 55(1), 410–450. ISSN 15333868. doi: 10.2514/1.C034442.

[10] Mannarino, A., Dowell, E. H., and Mantegazza, P. (2017). An adaptive controller for nonlinear flutter suppression and free-play compensation. *JVC/Journal of Vibration and Control*, 23(14), 2269–2290. ISSN 17412986. doi:10.1177/1077546315613935.

[11] Platanitis, G. and Strganac, T. W. (2004). Control of a Nonlinear Wing Section Using Leading- and Trailing-Edge Surfaces. *Journal of Guidance, Control, and Dynamics*, 27(1), 52–58. ISSN 07315090. doi:10.2514/1.9284.

[12] Mattaboni, M., Quaranta, G., and Mantegazza, P. (2009). Active flutter suppression for a three-surface transport aircraft by recurrent neural networks. *Journal of Guidance, Control, and Dynamics*, 32(4), 1295–1307. ISSN 15333884. doi:10.2514/1.40774.

[13] Wang, X., van Kampen, E., Chu, Q., et al. (2019). Stability Analysis for Incremental Nonlinear Dynamic Inversion Control. *Journal of Guidance, Control, and Dynamics*, 42(5), 1116–1129. ISSN 0731-5090. doi:10.2514/1.G003791.

[14] Wang, X., Van Kampen, E., Chu, Q., et al. (2019). Flexible aircraft gust load alleviation with incremental nonlinear dynamic inversion. *Journal of Guidance, Control, and Dynamics*, 42(7), 1519–1536. doi:10.2514/1.G003980.

[15] Wang, X., Mkhoyan, T., Mkhoyan, I., et al. (2021). Seamless Active Morphing Wing Simultaneous Gust and Maneuver Load Alleviation. *Journal of Guidance, Control, and Dynamics*, 44(9), 1649–1662. doi:10.2514/1.G005870.

[16] Dimitriadis, G. (2017). *Introduction to nonlinear aeroelasticity*. John Wiley & Sons.

[17] Fradkov, A. L., Miroshnik, I. V., and Nikiforov, V. O. (1999). *Nonlinear and Adaptive Control of Complex Systems*. Dordrecht: Springer Netherlands, vol. 491 ed. ISBN 978-90-481-5294-0. doi:10.1007/978-94-015-9261-1.

[18] Khalil, H. K. (2002). *Nonlinear Systems*. New Jersey: Prentice-Hall.

[19] Schildkamp, R., Chang, J., Sodja, J., et al. (2022). Development of an active aeroelastic parametric wing apparatus. In *International Forum on Aeroelasticity and Structural Dynamics 2022, IFASD 2022*, June. Madrid.

[20] Gjerek, B., Drazumeric, R., and Kosel, F. (2014). A Novel Experimental Setup for Multi-parameter Aeroelastic Wind Tunnel Tests. *Experimental Techniques*, 38(6), 30–43. ISSN 07328818. doi:10.1111/j.1747-1567.2012.00839.x.

[21] Theodorsen, T. (1935). Report No. 496, general theory of aerodynamic instability and the mechanism of flutter. *Journal of the Franklin Institute*, 219(6), 766–767. ISSN 00160032. doi:10.1016/S0016-0032(35)92022-1.

[22] Geertsen, J. A. (2020). *Development of a Gust Generator for a Low Speed Wind Tunnel*. Master's thesis, ETH Zürich.

[23] Hargrove, W. J. (1975). The C-5A Active Lift Distribution Control System. In *Proceedings of NASA Sponsored Symposium on Advanced Control Technology and Its Potential for Future Transport Aircraf*. National Aeronautics and Space Administration, pp. 325–351.